JOURNAL OF PROPULSION AND POWER
Vol. 20, No. 5, September–October 2004

Rotor-Generated Vane Row Off-Design Unsteady Aerodynamics Including Dynamic Stall, Part 1

Nicole L. Key,* Patrick B. Lawless,† and Sanford Fleeter‡
Purdue University, West Lafayette, Indiana 47907-2014

Off-design unsteady aerodynamics is addressed, including dynamic stall due to the interaction of rotor-generated wakes with a downstream vane row. This is accomplished when detailed rotor–stator unsteady aerodynamic blade row interaction data are obtained in a low-speed axial-flow research compressor. Experiments directed at time-variant particle image velocimetry measurements of the downstream stator flowfield, at negative incidence angles typical of part speed operation of the later stages of a high-pressure compressor, are described. Two stator stagger angles are investigated. A stator stagger angle of −17 deg provides a classic dynamic stall condition. At a more negative stagger of −22 deg, a steady separation is modulated by the wake pass event and also results in a shed vortex structure. The generation and subsequent shedding of the dynamic stall vortex is accompanied by flow separation and reattachment as a rotor traverses the stator passage.

Nomenclature

i = incidence angle
U = axial velocity
U' = axial velocity perturbation
V = tangential velocity
V' = tangential velocity perturbation
α = angle of attack
Ψ = stagger angle

Introduction

FOR an airfoil in a steady flow, the lift increases approximately linearly for small angles of attack, with the drag also increasing. However, at a critical angle of attack, the lift starts to decrease, the flow separates, and the airfoil is said to stall, with the critical angle of attack termed the steady or static stall angle.

Dynamic stall, an unsteady flow phenomenon, refers to unsteady flow separation with the airfoil transitioning in and out of stall. For an airfoil oscillating in torsion, dynamic stall typically begins at an angle of attack greater than the static stall angle, that is, the flow dynamics delay the onset of stall. Thus, an oscillating airfoil can exceed the steady stall angle without flow separation, which results in additional unsteady lift.

This additional unsteady lift is associated with a vortex that forms on the airfoil during the pitching motion. For an airfoil at moderate angle of attack, the flow around the airfoil is essentially inviscid. As the angle of attack increases, signs of boundary-layer separation begin at the trailing edge and move toward the leading edge. A vortex forms near the leading edge, grows, and convects downstream along the airfoil. This is accompanied by a significant lift overshoot, followed by flow separation, an increase in pitching moment, and a subsequent flow reattachment starting at the leading edge.[1] Figure 1 shows an isolated airfoil at different stages of positive incidence dynamic stall. This behavior takes the form of a limit cycle, with the time–mean angle of attack and lift at stall sometimes exceeding that experienced in steady flow.

Carr and McCroskey[2] reviewed experimental efforts to understand dynamic stall and computational efforts to predict dynamic stall. Particle image velocimetry (PIV) measurements have been made to examine the vorticity of the flow near an isolated airfoil in dynamic stall. Three main parameters that affect dynamic stall are transition, compressibility, and three-dimensional effects. The parameters that challenge computational fluid dynamics prediction of dynamic stall are turbulence modeling and numerical diffusion. Zaman et al.,[3] investigated dynamic stall on a periodically pitched airfoil. They obtained a lift hysteresis loop by measuring the velocity distribution in the wake. The unsteady lift on the airfoil was calculated by estimation of the change in circulation over time caused by the vorticity flux shed into the wake. Gendrich et al.[4] also investigated dynamic stall on a rapidly pitched airfoil, with focus on how the acceleration period at the start of the constant pitch rate trajectory of the airfoil impacted the dynamic stall behavior.

Unlike helicopter rotors, which execute pitching motions as they rotate, turbomachine rotor blades maintain a fixed angle of attack or incidence as they rotate. However, turbomachinery airfoils are subjected to periodically varying incidence angles as they cut through the wakes generated by upstream blade rows. For example, for one complete revolution of a subsonic turbomachine rotor, Fig. 2 shows that the rotor wakes manifest themselves mainly as absolute flow angle fluctuations in the reference frame of the downstream stator, with downstream vane incidence angles fluctuating from −15.0 to +1.9 deg over one rotor revolution, a considerable fluctuation (Sanders and Fleeter[5]).

The classical situation for study of the fundamentals of dynamic stall utilizes an oscillating isolated airfoil in a steady flow. Such studies have revealed that the primary condition for the onset of dynamic stall is a large variation in incidence or angle of attack. Clearly, this condition exists in turbomachinery blading, with the resulting unsteady blade row aerodynamics potentially leading to flow-induced vibrations and high cycle fatigue.

When a multistage compressor is operating at part-speed conditions, the front stages are typically at high positive mean incidence, whereas the rear stages are at low negative mean incidence. Thus, in the rear stages, rotor wake impingement on a downstream stator row can actually cause the vane to recover from an existing stalled condition or induce a periodic negative incidence separation. Because the frequency of rotor wake impingement is relatively high, the reduced frequency is greater than unity, which indicates that unsteady flow effects dominate the flow physics. Classic approaches to predicting unsteady lift on an airfoil do not model the decidedly nonlinear airfoil response of a dynamic stall condition.

Presented as Paper 2002-3542 at the AIAA Propulsion Conference, Indianapolis, Indiana, 2 July 2003; received 15 July 2003; revision received 15 December 2003; accepted for publication 15 December 2003. Copyright © 2004 by the authors. Published by the American Institute of Aeronautics and Astronautics, Inc., with permission. Copies of this paper may be made for personal or internal use, on condition that the copier pay the $10.00 per-copy fee to the Copyright Clearance Center, Inc., 222 Rosewood Drive, Danvers, MA 01923; include the code 0748-4658/04 $10.00 in correspondence with the CCC.

*Research Assistant, School of Mechanical Engineering. Student Member AIAA.
†Associate Professor, School of Mechanical Engineering. Member AIAA.
‡McAllister Distinguished Professor, School of Mechanical Engineering. Fellow AIAA.

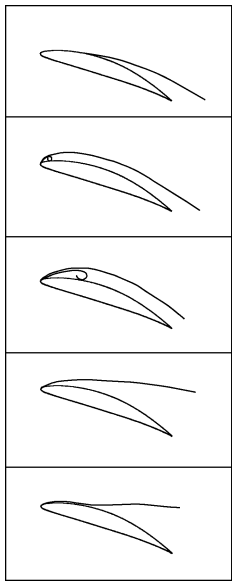

Fig. 1 Schematic of isolated airfoil in different stages of dynamic stall.

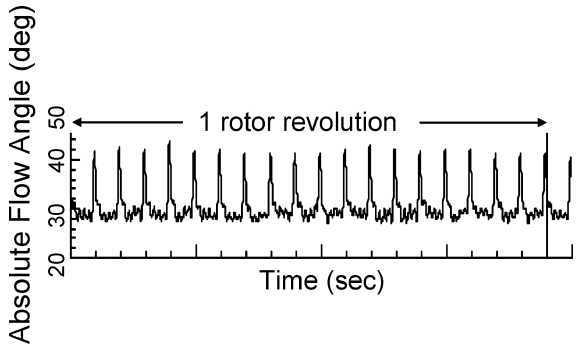

Fig. 2 Inlet flow angle to stator downstream of a subsonic turbomachine rotor.[5]

Dynamic stall has been previously encountered in studies in the Purdue Annular Cascade Research Facility. Henderson and Fleeter[6] investigated the unsteady stator pressure response to a large vortical wake generated by perforated plate rotors. Comparisons of the time mean of the unsteady lift to the steady-flow lift for the stators provided evidence for a negative incidence dynamic stall condition.

Motivated by the evidence provided in the previous investigation, this two-part paper is directed at the investigation of multistage interaction effects on airfoil unsteady aerodynamics, particularly at off-design operating conditions. The specific problem addressed is off-design unsteady aerodynamics, including dynamic stall due to the interaction of rotor-generated wakes with a downstream vane row. This is accomplished by means of detailed rotor–stator unsteady aerodynamic blade row interaction data obtained in a low-speed axial-flow research compressor. These detailed data include measurements of the rotor wake generated unsteady aerodynamic forcing function to the downstream stator, the resultant stator vane steady and unsteady aerodynamic response, and PIV measurements of the time-variant stator midspan vane-to-vane flowfield. This portion of the paper describes the time-variant PIV measurements of the downstream stator flowfield, with the rotor wake generated forcing function and downstream stator steady and unsteady aerodynamic response data described in the companion paper.[7]

Research Facility

The Purdue Annular Cascade Research Facility (Fig. 3) is an open-loop drawthrough wind tunnel with a maximum test section velocity of 220 ft/s (67.06 m/s). A honeycomb section and acoustically treated inlet plenum condition the flow before it is accelerated through a bellmouth and enters the test section. After the flow exits the test section, it enters a diffuser and then discharges into a large plenum. Downstream of the plenum, a centrifugal blower powered by a 300-hp (223.7-kW) induction motor draws the air through the test section. Damper vanes upstream of the blower adjust the flow rate through the facility. In the test section, a 50-hp (37.28-kW) dc motor powers an axial-flow rotor with the rotor speed controlled by a variable speed drive. Because the primary energy source to the flow is the downstream blower, the axial velocity through the test section can be set independently from the rotor speed.

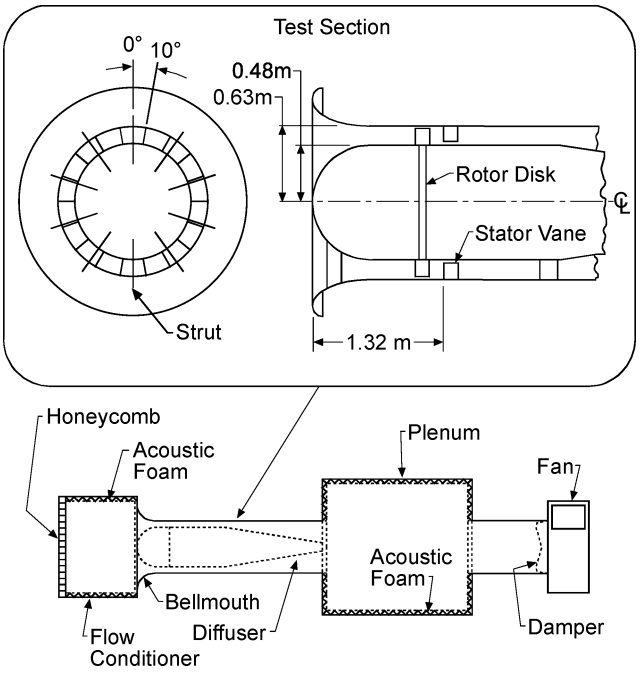

Fig. 3 Purdue annular cascade research facility.

The rotor blades are attached to a T slot, machined into the hub of the rotor disk, via sliding cars to allow the spacing and number of blades to be varied. For this experiment, 19 rotor blades, at a stagger angle of −30 deg at midspan, are evenly spaced around the annulus with an angular displacement of 18.95 deg between blades. The rotor airfoil profile is a NACA 65A010 thickness distribution superimposed on a NACA $a = 1.0$ uniform load meanline. The blades have 8.2 deg of twist from hub-to-tip with a chord of 5.0 in. (12.7 cm) and span of 5.9 in. (14.99 cm).

The stator configuration has 18 vanes uniformly spaced with an angular displacement of 20 deg between vanes. The stator vanes are constructed with a NACA 65A012 thickness distribution on a 30-deg circular arc meanline. The chord and span are 6.0 in. (15.4 cm), with the stator stagger angle varied to achieve different stator mean loading levels.

PIV Data Acquisition and Analysis

Ehrlich and Fleeter[8] were the first to acquire PIV data in the Purdue Annular Cascade Research Facility. PIV is a measurement technique that obtains instantaneous, quantifiable information of an entire two-dimensional flowfield. A laser beam is passed through an optical train consisting of mirrors and lenses to produce a laser light sheet that illuminates a two-dimensional plane of interest. The flowfield is seeded with tracer particles that follow the flow, and a charge-coupled device (CCD) camera records images of the illuminated particles in the light sheet. The laser is double pulsed, and the camera records two back-to-back images. These images are divided into rectangular interrogation regions for processing into velocity information. A cross-correlation technique is used to determine the average displacement vector for each region. When the displacement and the time between laser pulses are known, the velocity field is obtained.

The Dantec PIV system utilized for this experiment consists of a 100-mW New Wave Research Minilase Gemini PIV Nd:YAG laser, a high-resolution Kodak Megaplus ES 1.0 digital camera, and a PIV-2100 Processor controlled by a personal computer. The laser has twin oscillators that provide two high-energy pulses within the short time delay provided by the software. The laser operates at a wavelength of 532.0 nm (visible green light), a repetition rate of 15 Hz, and a pulse width of 10.0 ns. The digital camera has a 1008 by 1018 CCD array. It is operated in cross-correlation mode so that the first image is stored while the second image is acquired. Both images are transferred to the PIV-2100 processor, providing real-time calculation of the velocity vector field. The PIV-2100 processor also synchronizes the camera, laser, and external trigger provided from the shaft of the rotor.

Accurate PIV measurements depend on proper seeding of the flowfield. The particles must be small enough to follow the flow and also be large enough to scatter an appropriate amount of light for the camera. A Rosco 1600 fog machine is used to generate seed particles from a propylene glycol-based fog solution. As the fluid is discharged into the atmosphere, it vaporizes and condenses into a fine mist of particles. The particles are introduced into the air upstream of the facility inlet, which provides a sufficiently uniform dispersion of particles to the test section. The fog machine produces a large number of particles, ranging in size from 0.5 to 5.0 μm, by the heating of the pressurized glycol-based fog fluid. Guidelines established by Samimy and Lele[9] were used to ensure that the tracer particles reasonably follow the flow. The guidelines state that for optical techniques, such as PIV, the velocity measurement errors grow linearly with the ratio of the seed particle response time based on Stokes drag to the flow timescale, with approximately 2% error for a ratio of 0.2. For this experiment, the length scale of interest is associated with the dynamic stall vortex, and the ratio of seed particle response time to flow time scale is 0.14, indicating that a measurement error less than 2% is associated with seed particle tracking.

The instantaneous stator vane-to-vane flowfield is measured at 50% span for several time instants as the upstream rotor traverses the stator passage of interest. A once-per-revolution pulse from a photo-optic sensor on the rotor shaft is sent to the PIV-2100 processor that prompts the camera to acquire CCD images when the laser pulse and shaft trigger coincide. The trigger is set when a specific rotor aligns with the lower stator of the passage of interest. To obtain images when the rotor is traversing the passage, the measured rotor speed is used to calculate the time after the trigger when the rotor will be at a certain angular position. For this, the trigger signal is fed into a BNC Model 500 pulse generator. A time delay is input into the pulse generator, and the output from the pulse generator is fed into the PIV-2100 processor.

The stator vane-to-vane flowfield is examined at 50% span with a 1-mm-thick light sheet introduced downstream of the stators via a probe that enters the flowfield through an opening in the casing of the cascade. Figure 4 shows the PIV optics layout based on the design by Ehrlich and Fleeter.[8] Three cylindrical lenses produce the light sheet. The first two lenses set the focal length such that the light sheet will be at its thinnest in the region of interest. The last lens expands the beam into a diverging light sheet that is wide enough to illuminate the entire stator passage. Optical access to the stator passage is obtained with a $\frac{3}{4}$-in.-thick Plexiglas® window. The camera is set perpendicular to the light sheet. A Nikkor 60-mm focal length lens is attached to the camera to sample the entire passage.

The images corresponding to each laser pulse are divided into rectangular interrogation regions small enough such that the velocity of the particles is homogenous. However, the region must also be large enough to have a statistically sufficient number of particles to sample. To increase the signal-to-noise ratio, the interrogation regions are overlapped, effectively oversampling the data. Although it does not increase the spatial resolution, overlapping interrogation regions provides additional vectors as valid interpolated vectors. For these experiments, the interrogation regions are 32 by 32 pixels with 50% overlap, providing 3844 raw vectors per image.

Vectors are validated based on correlation peak height and vector range. The PIV-2100 processor generates a correlation plane where

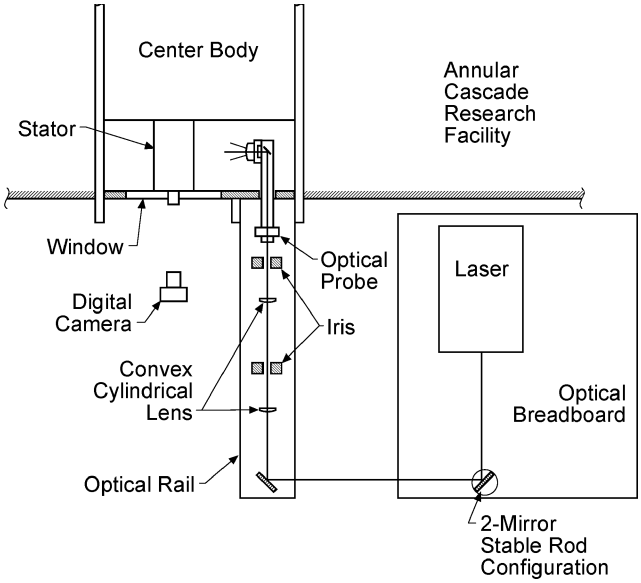

Fig. 4 PIV optics layout.

Fig. 5 Raw PIV image at stator stagger of −17 deg at RRP = 50%.

high correlation peaks indicate that many of the particles match their corresponding spatially shifted partners in the second frame. Low correlation peaks indicate that most of the individual particles match with other particles. The PIV-2100 processor locates the highest and second highest peaks in the correlation plane. Peak-height validation requires that the ratio of the highest peak to the second highest peak must be at least 1.2. Range validation then restricts the minimum and maximum vector lengths to a specified range. Invalid vectors occur if an interrogation region does not have sufficient seeding, if the light sheet causes a reflection off of a surface such as the vane, or if the particle travels out of the plane of the light sheet between frames. The uncertainty in velocity based on displacement errors due to pixel resolution of the image and error in locating the image displacement peak using the cross-correlation technique is estimated to be $\pm 8\%$ of the uncertainty with the method described by Huang et al.[10] This is an acceptable level of uncertainty because the flow features are of interest, whereas the magnitude of velocity is of secondary importance.

With 18 stators, there is an angular distance of 20 deg between each stator. Data are acquired in rotor relative position (RRP) increments of 10% vane passage (2-deg increments), with the triggered rotor blade position designated as RRP = 0%. After the off-line validation is performed, a representative ensemble-averaged velocity vector map is obtained for each RRP.

Figure 5 shows an image obtained using the PIV system for a stator stagger of −17 deg at RRP = 50%. Note that the dynamic

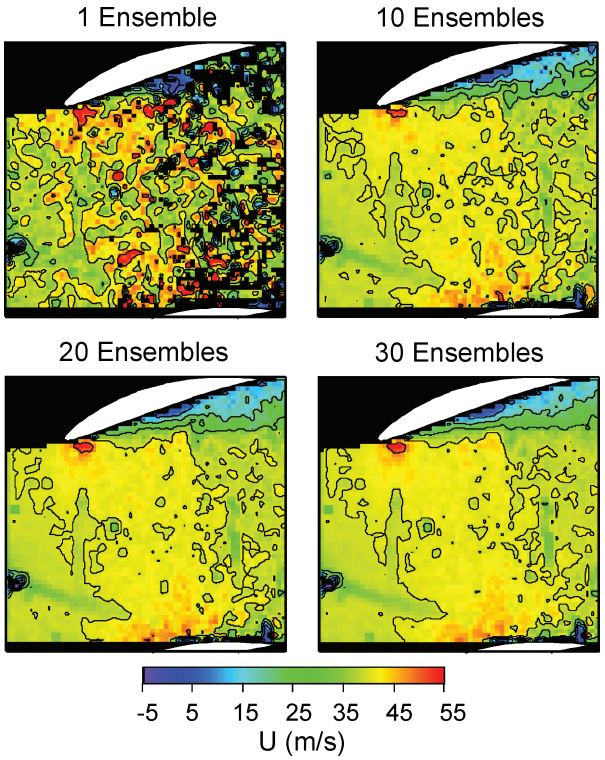

Fig. 6 Axial velocity ensemble averaging.

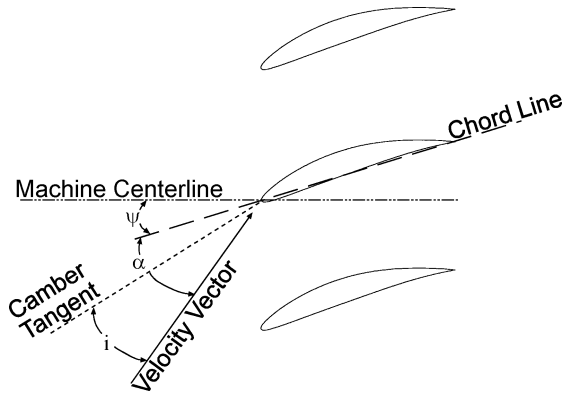

Fig. 7 Stator vane and flow geometry.

stall phenomenon will occur on the nominal pressure side of the vanes because they are set at negative incidence. Also, a portion of the lower stator in the passage is included in the field of view for reference.

The effect of using different numbers of images for ensemble averaging is demonstrated in the axial velocity plots of Fig. 6. The instantaneous image for one ensemble shows many interrogation region black areas that are invalid vectors. When 30 ensembles are used, a clean snapshot of the flowfield is obtained where the random unsteadiness has been averaged out. Very little difference exists between the images for 20 ensembles and 30 ensembles. For the remaining plots, 30 images are used for ensemble averaging, and each interrogation region must have at least 10 valid vectors to register a valid mean velocity.

For these experiments, the mass flow and the rotor speed are maintained constant, with the stator stagger angle set at ψ of -17 and -22 deg. The stator geometry including the stator stagger angle ψ, the angle of attack α, and the incidence angle i are shown in Fig. 7.

Results

The vane passage axial and tangential velocity components, U and V, for RRP = 0% are presented in Fig. 8. Recall that the light

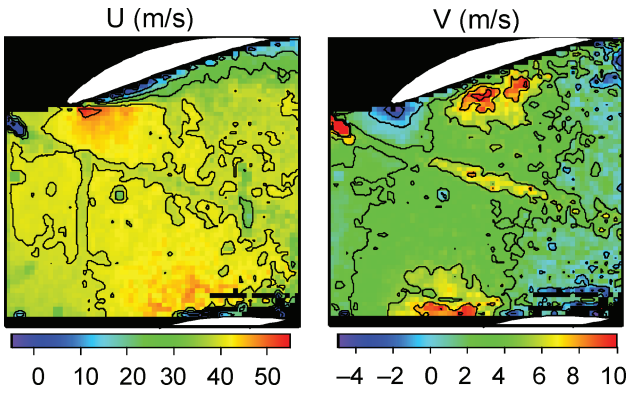

Fig. 8 Axial and tangential velocities for stator stagger of −17 deg at RRP = 0%.

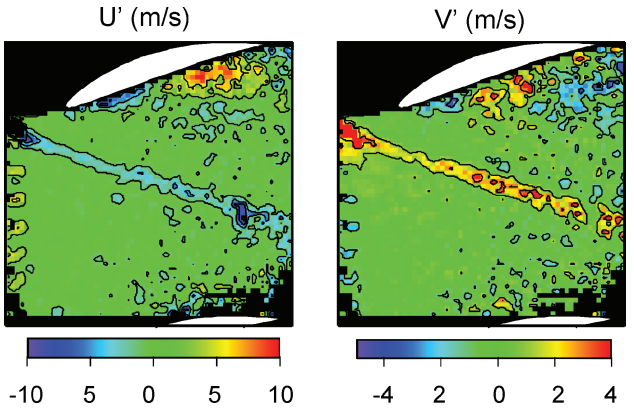

Fig. 9 Axial and tangential perturbation velocity for stator stagger of −17 deg at RRP = 0%.

sheet is introduced downstream of the stator and projected upstream, with all velocity data ensemble averaged. The rotor blade wake is visible in Fig. 8 as a region extending from the rotor blade trailing edge, characterized by a decrease in axial velocity and an increase in tangential velocity. The negative tangential velocity on the vane pressure surface near the leading edge indicates that the stagnation point is on the vane suction surface, as expected at negative incidence. This is also responsible for the strong acceleration in the axial velocity at the leading edge on the pressure surface.

The perturbation velocity field highlights the wake shed from the upstream rotor blade. Figure 9 shows the axial U' and tangential V' perturbation velocities in the vane passage. These values are obtained when the vector maps for measurements at all of the rotor positions are first averaged, thereby characterizing the time-average velocity field. This time-average velocity field is then subtracted from the ensemble-averaged vector map for the single rotor position of interest. Note that the periodic structures at the left-hand side of the perturbation fields are artifacts of the rotor blade trailing-edge surface present in the images that comprise the time-average map and not actual flow features.

The rotor blade wake is relatively thin, with the wake width slightly increasing with distance from the rotor blade trailing edge. It also becomes somewhat less coherent as dissipation occurs. The ensemble-average rotor blade wake has a positive tangential perturbation velocity. In the reference frame of the downstream stator, the wake fluid has a higher tangential velocity component than the freestream (Fig. 10). This slip velocity causes the low momentum wake fluid to drift across the vane passage and to collect on the airfoil pressure surface as the chopped wake segments are transported downstream. As the low momentum wake fluid accumulates on the airfoil pressure surface, it will interact with the airfoil boundary layer and eventually end up appearing in the wakes of the blade row that performs the chopping. The negative axial perturbation velocities near the pressure surface of the blade highlight the region of weak/separated flow associated with the dynamic stall phenomenon.

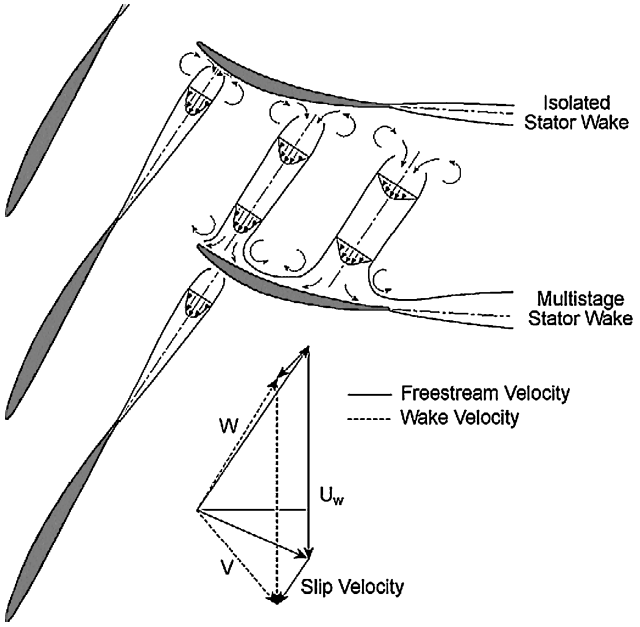

Fig. 10 Schematic of wake slip velocity.

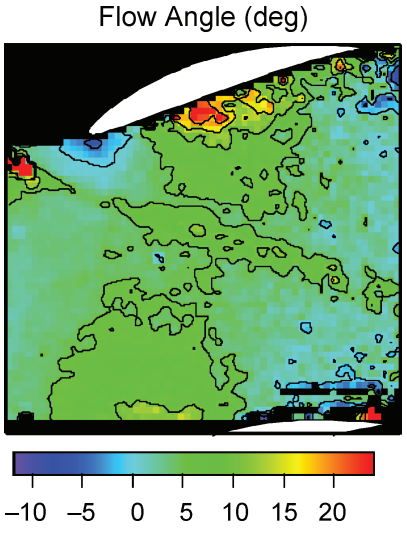

Fig. 11 Flow angle for stator stagger of −17 deg at RRP = 0%.

Negative and positive tangential perturbation velocities associated with the dynamic stall vortex also characterize the pressure surface of the blade.

The vane passage flow angle variation for the RRP = 0% case is shown in Fig. 11. At the leading-edge plane, the vane mean incidence angle is 3.7 deg. This corresponds to a vane incidence angle of −28.3 deg. The absolute flow angle varies along the passage inlet plane from −7.2 deg near the leading edge on the pressure surface to +8.9 deg near the bottom of Fig. 11. A tangential cut through the wake near the center of the vane passage shows that the center of the wake has a maximum flow angle of 9.7 deg, whereas the edges of the wake return to 4.2 deg. Thus, there is a large variation in vane incidence due to the unsteady flow generated by the rotor blades. Hence, although the classical situation for studying dynamic stall addresses an oscillating airfoil in a steady flow, conditions for dynamic stall, a large variation in incidence or angle of attack, exists in this research compressor.

Figure 12 shows the normal vorticity calculated from the ensemble-averaged velocity data in the vane passage. The algorithm used to calculate vorticity implements a second-order centered differencing technique. Vorticity is not calculated for an interrogation region unless valid vectors surround it on all four sides. The rotor blade wake shows negative vorticity off the rotor pressure surface and positive vorticity off the suction surface, with the rotor blade wake defined by the band of positive and negative vorticity. The wake vorticity strength does not appear to be decaying, but the bands of vorticity become less coherent as the rotor blade wake travels through the vane passage. The pressure surface of the stator shows high positive vorticity near the leading edge. This is a result of a separation bubble near the leading edge causing large velocity gradients in the flowfield.

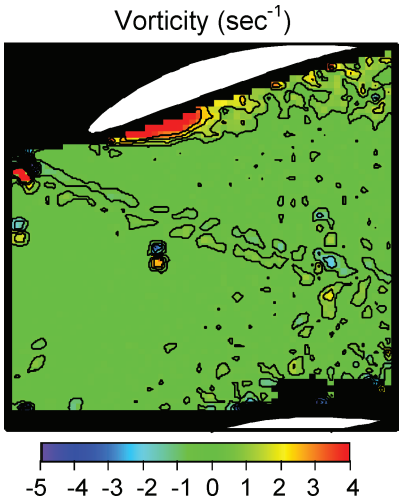

Fig. 12 Vorticity for stator stagger of −17 deg at RRP = 0%.

Because dynamic stall is a periodic flow phenomenon, it is helpful to consider the variations with time of the kinematic flow descriptors. Figure 13 shows the vane passage vorticity as the rotor traverses the passage. A transient separation bubble forms at the leading edge of the vane pressure surface, with the collapse of this bubble over the cycle giving rise to a shed vortex structure. At RRP = 40%, the vortex starts to convect downstream. At RRP = 70%, the dynamic stall vortex has been shed, and the flow over the vane is reattached. Then, at RRP = 80% and RRP = 90%, the leading-edge vortex develops, it becomes stronger, and the whole process repeats. Note that data are taken at RRP = 100% also, which corresponds to the RRP = 0% for the next rotor blade.

At RRP = 10%, the rotor blade wake impinges on the vane leading edge. The negative vorticity in the wake cancels some of the positive vorticity in the separation bubble, which causes the region of high vorticity in the separation bubble to decrease slightly in size. After this RRP, the rotor wake rapidly decays and loses its initial band shape. The chopped wake segment in RRP = 10% appears to be wider than the wake in RRP = 0%. This rotor wake flow migrates toward the vane pressure surface from RRP = 10% to RRP = 40%, where the accumulation of the wake flow appears to have concentrated on the aft part of the airfoil. The rotor wake fluid ends up in the stator wake. The rotor wake in RRP = 0% appears to be bowed with respect to the rotor blade wake at RRP = 90%. This could be caused by the higher convection velocity near midpassage as compared to that near the leading-edge stagnation point. Note that the patches of permanent vorticity appearing near the center of the vane passage are created by dimples in the window.

Figure 14 shows the vane passage axial velocity as the rotor traverses the passage. The separated flow region can be tracked as the dark blue region near the vane. The flow reattaches near the leading edge as the vortex moves toward the trailing edge. This is seen at RRP = 50%, where the separation bubble is near midchord. At RRP = 70%, the flow is reattached. At RRP = 90%, a separation bubble forms at the leading edge, and the process repeats. The accumulation of low momentum fluid occurs on the aft part of the vane. At RRP = 10%, the region of low momentum fluid on the aft part of the vane is relatively thin, but it increases up to RRP = 50%, where this region covers about 20% of the vane passage, almost doubling in size. In RRP = 80% and 90%, this low momentum fluid from the rotor blade wake becomes part of the vane wake fluid.

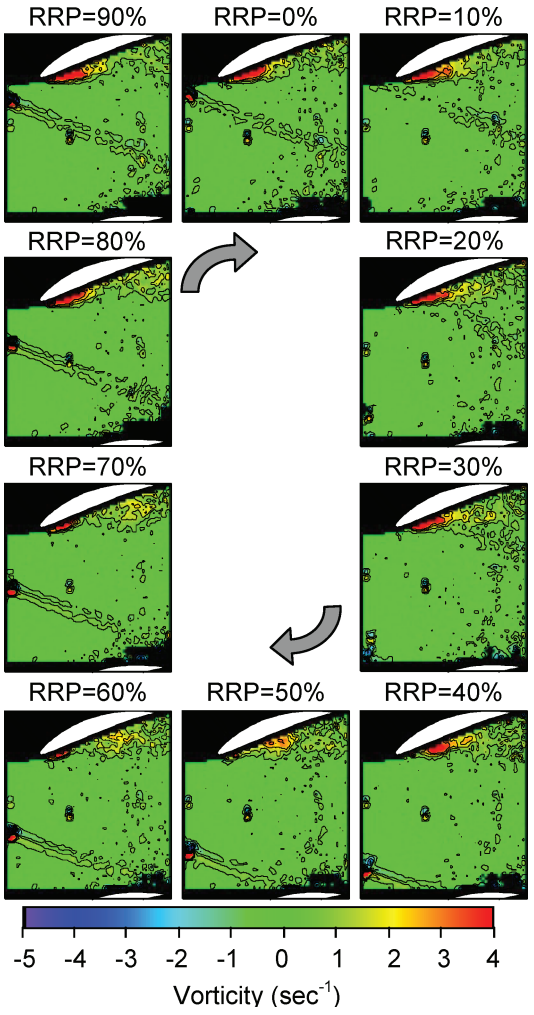

Fig. 13 Vorticity for stator stagger of −17 deg as rotor traverses stator passage.

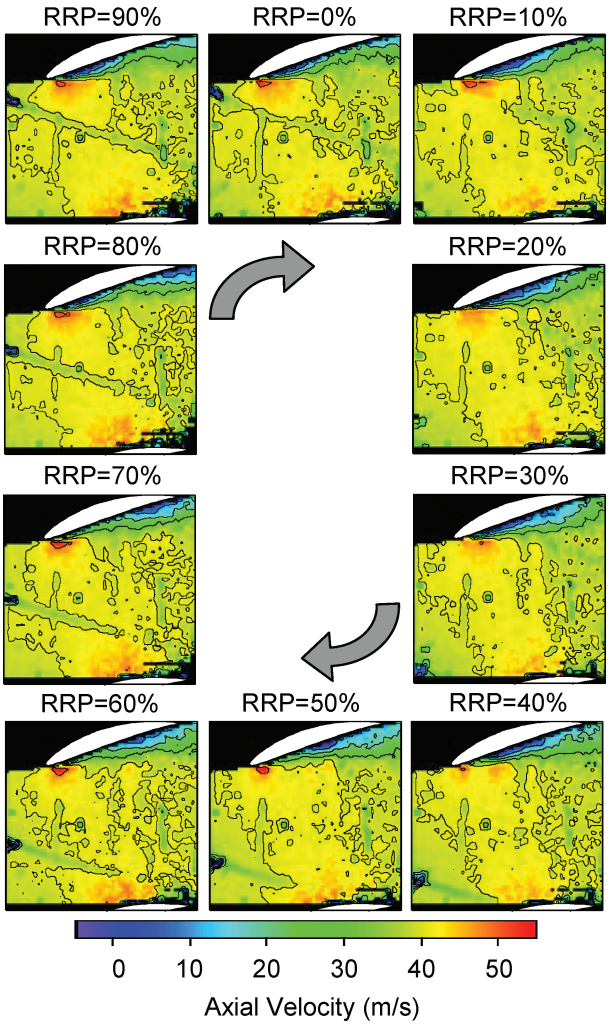

Fig. 14 Axial velocity at stator stagger of −17 deg as rotor traverses stator passage.

The downwash velocity, defined as the perturbation velocity perpendicular to the vane chordline near the surface, is presented in Fig. 15. In linear unsteady aerodynamic theory, this downwash velocity is the driver for the unsteady static pressure on the airfoil and, thus, the unsteady lift on the airfoil. Figure 15 tracks the downwash on the vane as the rotor blade traverses the vane passage. The velocity perturbation associated with the wake is the source of the downwash velocity perturbation. However, as shown, a large disturbance here appears to track the separation region seen earlier in Fig. 14. A negative dip in the downwash first appears at RRP = 30%, then moves down the vane through RRP = 80%. This event clearly overwhelms any perturbation associated with the rotor blade wake passage and, thus, identifies the dynamic stall event itself as the primary driver for the unsteady lift.

Results are also investigated for a vane stagger angle of −22 deg. Figure 16 shows a comparison of the axial velocity for vane stagger angles of −17 deg and stagger of −22 deg for the same RRP. The scale has been adjusted for this comparison. At a vane stagger of −22 deg, there is always a larger leading-edge separation, with the flow never reattaching as it does for the vane stagger of −17 deg at RRP = 70%. Rather, the rotor blade wake passage event appears to modulate slightly the extent of the separation zone. With a stator stagger of −22 deg, the vane passage area has decreased because of the more negative stagger and the separated flow, causing an increase in the passage velocity. Also, at the more negative stagger, the stagnation point is farther away from the leading edge along the suction surface. The permanent leading edge separation bubble seen in stagger of −22 deg is followed by a larger region of lower momentum fluid at all RRP.

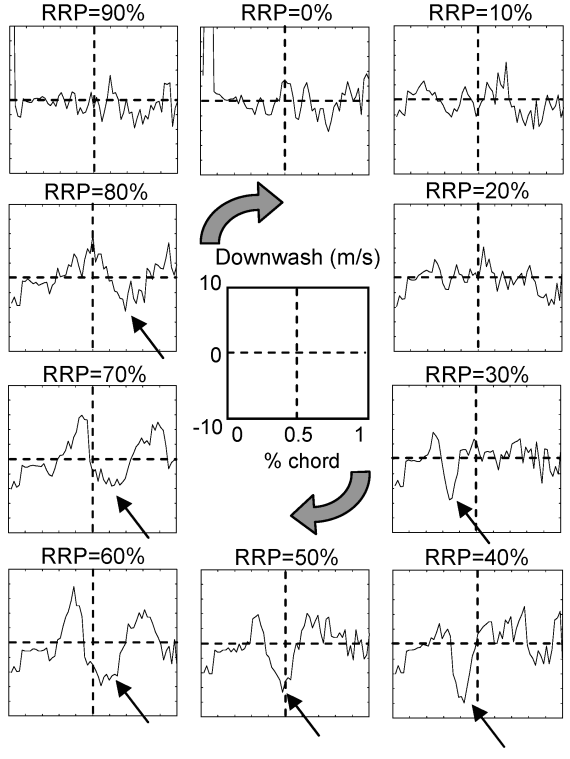

Fig. 15 Downwash at various RRP at stator stagger of −17 deg.

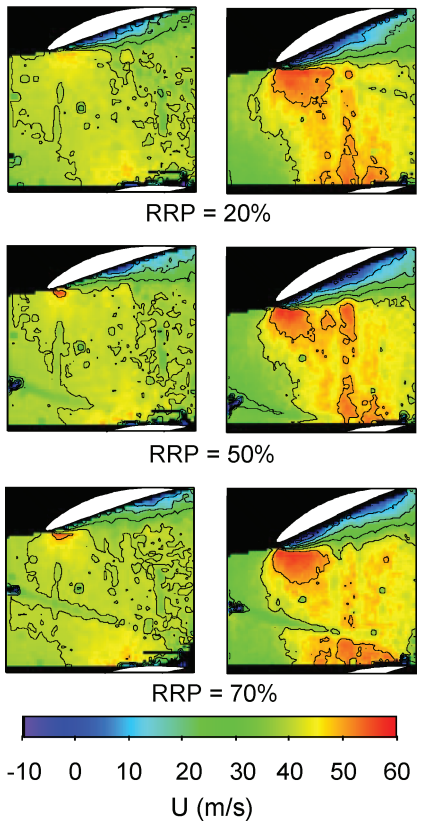

a) Stagger = −17 deg b) Stagger = −22 deg

Fig. 16 Axial velocity at stator stagger angles of −17 and −22 deg.

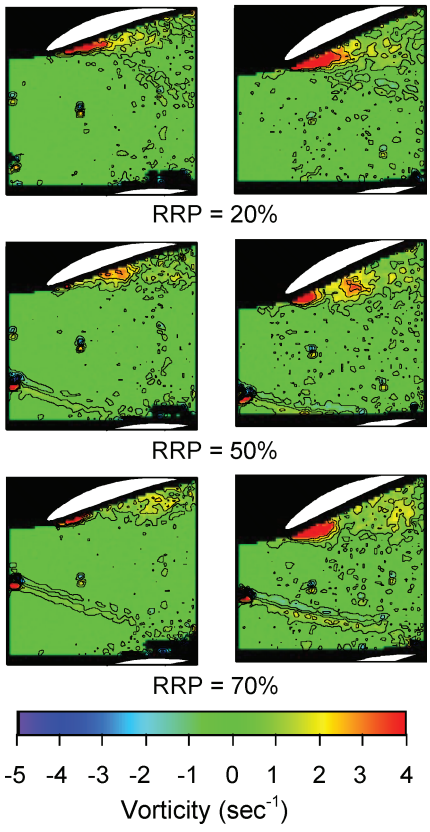

a) Stagger = −17 deg b) Stagger = −22 deg

Fig. 17 Vorticity at stator stagger angles of −17 and −22 deg.

Figure 17 makes the same comparisons for the vorticity. The stator stagger of −22 deg has a stronger leading-edge separation that always remains at the leading edge. A vortex of greater strength is shed in this case than that seen at −17 deg stagger. The rotor blade wake is wider, and the vorticity in the wake is also stronger for the −22 deg stagger. The region of positive vorticity, corresponding to low momentum fluid, near the trailing edge of the vane on the pressure surface extends over 25% of the vane passage for all RRP rather than modulating from nearly zero thickness to 15% of the vane passage as seen in the −17 deg stagger case.

Conclusions

The specific problem addressed is off-design unsteady aerodynamics including dynamic stall due to the interaction of rotor-generated wakes with a downstream vane row. This is accomplished by obtaining detailed rotor–stator unsteady aerodynamic blade row interaction data in a low-speed axial-flow research compressor. In this paper, experiments directed at time-variant PIV measurements of the downstream stator flowfield at negative incidence angles typical of part-speed operation of the later stages of a high-pressure compressor are described.

Two stator stagger angles are investigated. A stator stagger angle of −17 deg provides a classic dynamic stall condition. At a more negative stagger of −22 deg, a steady separation is modulated by the wake pass event and also results in a shed vortex structure. The generation and subsequent shedding of the dynamic stall vortex is accompanied by flow separation and reattachment as a rotor traverses the stator passage.

In classic theory, the velocity perturbation associated with the wake is the source of the forcing function for unsteady lift and HCF. However, at off-design points, the compressor blades often operate at mean incidence angles close to the stall point and, thus, can exhibit dynamic stall behavior. As shown in these experiments, the dynamic stall event clearly overwhelms any perturbation associated with wake passage thus suggesting this phenomenon as a primary contributor for blade HCF.

Acknowledgments

This research was sponsored by the NASA John H. Glenn Research Center at Lewis Field and the U.S. Air Force Office of Scientific Research. This support is most gratefully acknowledged.

References

[1]Reynolds, W. C., and Carr, L. W., "Review of Unsteady, Driven, Separated Flows," AIAA Paper 85-0527, March 1985.

[2]Carr, L. W., and McCroskey, W. J., "A Review of Recent Advances in Computational and Experimental Analysis of Dynamic Stall," *Proceedings of the International Union of Theoretical and Applied Mechanics Symposium on Fluid Dynamics of High Angle of Attack*, Sept. 1992.

[3]Zaman, K. B. M. Q., Panda, J., and Rumsey, C. L., "Estimation of Unsteady Lift on a Pitching Airfoil from Wake Velocity Surveys," AIAA Paper 93-0437, Jan. 1993.

[4]Gendrich, C. P., Koochesfahani, M. M., and Visbal, M. R., "Initial Acceleration Effects on the Flow Field Development Around Rapidly Pitching Airfoils," *Journal of Fluids Engineering*, Vol. 117, No. 1, 1995, pp. 45–49.

[5]Sanders, A., and Fleeter, S., "Multi-Blade Row Interactions in a Transonic Axial Compressor Part II: Rotor Wake Forcing Function and Stator Unsteady Aerodynamic Response," American Society of Mechanical Engineers, ASME Paper 2001-GT-0269, Jan. 2001.

[6]Henderson, G. H., and Fleeter, S., "Vortical Gust Response of a Low-Solidity Vane Row Including Steady Loading and Dynamic Stall Effects," *Journal of Turbomachinery*, Vol. 119, No. 3, 1997, pp. 482–490.

[7]Fulayter, R. D., Lawless, P. B., and Fleeter, S., "Rotor-Generated Vane Row Off-Design Unsteady Aerodynamics Including Dynamic Stall, Part 2," *Journal of Propulsion and Power*, 2004.

[8]Ehrlich, D. A., and Fleeter, S., "Particle Image Velocimetry Characterization of a Chordwise Bending Cascade Flowfield," *Journal of Propulsion and Power*, Vol. 18, No. 2, 2002, pp. 448–455.

[9]Samimy, M., and Lele, S. K., "Motion of Particles with Inertia in a Compressible Free Shear Flow," *Physics of Fluids A*, Vol. 3, No. 8, 1991, pp. 1915–1923.

[10]Huang, H., Dabiri, D., and Gharib, M., "On Errors of Digital Particle Image Velocimetry," *Measurement Science and Technology*, Vol. 8, No. 12, 1997, pp. 1427–1440.